

Rotating cylindrical magnetron sputtering: Simulation of the reactive process

D. Depla,^{1,a)} X. Y. Li,² S. Mahieu,¹ K. Van Aeken,¹ W. P. Leroy,¹ J. Haemers,¹
R. De Gryse,¹ and A. Bogaerts³

¹Department of Solid State Sciences, Research Group DRAFT, Ghent University, Krijgslaan 281 (S1), 9000 Gent, Belgium

²Department of Physics, Taiyuan University of Technology, 030024 Taiyuan, People's Republic of China

³Department of Chemistry, Research Group PLASMANT, University of Antwerp, Universiteitsplein 1, 2610 Wilrijk-Antwerp, Belgium

(Received 23 November 2009; accepted 4 April 2010; published online 7 June 2010)

A rotating cylindrical magnetron consists of a cylindrical tube, functioning as the cathode, which rotates around a stationary magnet assembly. In stationary mode, the cylindrical magnetron behaves similar to a planar magnetron with respect to the influence of reactive gas addition to the plasma. However, the transition from metallic mode to poisoned mode and vice versa depends on the rotation speed. An existing model has been modified to simulate the influence of target rotation on the well known hysteresis behavior during reactive magnetron sputtering. The model shows that the existing poisoning mechanisms, i.e., chemisorption, direct reactive ion implantation and knock on implantation, are insufficient to describe the poisoning behavior of the rotating target. A better description of the process is only possible by including the deposition of sputtered material on the target. © 2010 American Institute of Physics. [doi:10.1063/1.3415550]

I. INTRODUCTION

In contrast to a planar magnetron, the target of a rotating cylindrical magnetron rotates around the stationary magnet assembly.¹ In this way, the racetrack moves over the target, resulting in a more uniform target erosion. A first consequence is a much higher effective target consumption (70%–85%) compared to planar magnetrons. Hence, the down time of the industrial plant due to target replacement can be reduced.² A second consequence of the target rotation is a dependence of the transition point from metallic mode to poisoned mode on the rotation speed. This effect has been reported by several authors.^{3–6} Indeed, when a reactive gas is added to the discharge, the reactive gas partial pressure remains initially low due to the gettering of the reactive gas by the deposited target material. Further increasing the reactive gas flow, one reaches a critical gas flow where the reactive gas cannot be further consumed by the target material. Depending on the pumping speed, a more or less abrupt increase in the partial pressure is noticed. Simultaneously, other deposition parameters, as discharge voltage and deposition rate, also change. As the deposition rate drastically decreases, one identifies this regime as the *poisoned mode*. When the partial pressure of the reactive gas is low, and the deposition rate is high, the reactive sputtering process is in *metallic mode*. After the transition from metallic mode to poisoned mode, one needs to decrease the reactive gas flow beyond the first transition point to return to metallic mode, i.e., the deposition parameters as a function of the reactive gas flow show a hysteresis behavior with two transition points. The value of the reactive gas flow at the transition points depends on the target rotation speed. Increasing the

rotation speed shifts the transition points toward lower reactive gas flows, or stated differently, less oxygen is needed to poison the target at a higher rotation speed. In this study, we wish to model this behavior by improving a previously published model.⁷ The details of the model and the modifications are discussed in Sec. II. The most important modification is related to an extra mechanism, i.e., the deposition of sputtered material on the target. The importance of this effect was discussed earlier,⁸ and its implementation into the model is treated in this paper. In Sec. III, an overview of the input parameters is given. In Sec. IV, we confront this model with previously published experimental results, and a conclusion is given in Sec. V.

II. MODEL

The model describes the reactive sputtering process. The equations are presented in an alternative way, as compared to previous work.^{7,9} However, the equations fundamentally describe the same processes and the derivation has been described in detail in Refs. 7 and 9. This alternative way of presenting has been chosen to include the deposition of the sputter material on the target in a transparent way.

To describe the reactive sputter process, three important parts in the deposition setup can be distinguished as follows: the target, the substrate, and the vacuum chamber. For each part, one or more cells are defined, and continuity equations are used to describe the conservative transport of the relevant quantity. This approach will be made more clear in the following sections. These equations are solved using the finite difference method, with a time step of typically 5×10^{-2} ms, and are implemented in a user-friendly code, entitled RSD2009.¹⁰

^{a)}Electronic mail: diederik.depla@ugent.be.

A. The vacuum chamber

The vacuum chamber is described as one cell. Each part of the vacuum chamber on which target material is deposited, except for the target, is defined as the “substrate.” Reactive gas is introduced in the vacuum chamber at a given flow rate q_0 . The reactive gas leaves the chamber by three paths, i.e., by chemical reaction on the target, by chemical reaction with the sputtered material deposited on the substrate, and finally by the action of the vacuum pump. For each defined path, the gas is consumed at a given rate, i.e., q_t (for the target), q_s (for the substrate), and q_p for the pump. A continuity equation can be written for the cell describing the vacuum chamber,

$$\frac{dP}{dt} = \frac{k_B T}{V} [q_0 - (q_p + q_t + q_s)], \quad (1)$$

with V the chamber volume, k_B the Boltzmann constant, and T the temperature of the gas. The reactive gas partial pressure is given by P . This equation was derived from the ideal gas law, with the flow or gas consumption rates (q) defined as molecules per second ($q = dn/dt$). The gas consumption by the target, q_t , and by the substrate q_s , depend on the target condition and substrate condition, respectively, as will be described in the following sections. The gas consumption by the vacuum pump is given by

$$q_p = \frac{PS}{k_B T}, \quad (2)$$

with S the pumping speed for the deposition setup (in m^3/s).

Based on kinetic gas theory, the reactive gas partial pressure defines the flux of reactive gas molecules toward the substrate and the target (in molecules per m^2 and per second),

$$F = \frac{P}{\sqrt{2\pi m k_B T}}, \quad (3)$$

with m the mass of the gas molecule.

Based on the reactive gas partial pressure, the reactive gas fraction in the plasma can be calculated,

$$f = \frac{P}{P + P_{Ar}}, \quad (4)$$

with P_{Ar} the argon pressure. The model assumes that the number of reactive molecular ions which bombard the target is proportional to the reactive gas fraction given by Eq. (4). A further extension of the simulation could be the implementation of effective plasma composition¹¹ but at present the above assumption is used as a first approximation.

B. The substrate condition

At the substrate (see previous section for definition), target material is deposited according to a certain deposition profile and the reactive gas can become incorporated.¹² By subdividing the substrate in more lateral cells, as illustrated in Refs. 9 and 13, one can account for the real deposition profile, but for sake of simplicity the latter has not been implemented in the present paper. Hence, an uniform depo-

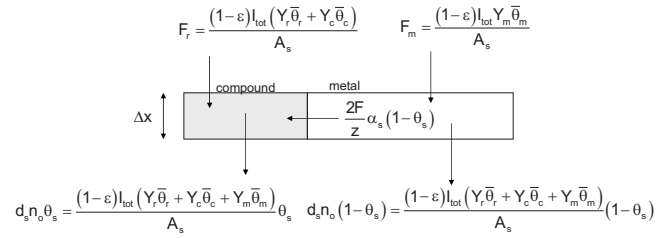


FIG. 1. Schematic representation of the substrate cell description. For the compound subcell (left) there are two incoming fluxes, i.e., the direct deposition of compound material F_r , and the compound formed by incorporation of reactive gas molecules during the deposition of the target material. The latter is indicated by the right-to-left arrow, because it is a loss of the metal fraction. The outgoing flux is controlled by the deposition rate d_s which is defined by the average target condition. For the metal subcell, the incoming flux is the deposition of metal F_m . The outgoing flux is defined by the deposition rate and the incorporation of reactive gas molecules as explained above. The thickness of the substrate cell is the height of one monolayer resulting in $\Delta x n_o = n_{o,s}$ with n_o the material density and $n_{o,s}$ the material surface density.

sition profile is assumed and the top layer of the substrate is defined by one cell. Again a continuity equation can be written. This means that one needs to identify the different (incoming and outgoing) fluxes of compound/metal, and the sources or the losses of compound/metal material. Figure 1 shows the relevant processes for the substrate cell.

We first focus on the incoming fluxes (top of Fig. 1). From the target, compound and metal is sputtered and arrives on the substrate. The compound flux F_r sputtered from the target arriving on the substrate is defined by the average fraction of compound on the target [given by $\bar{\theta}_r$ and $\bar{\theta}_c$, see further Sec. II C, Eq. (11)], the sputter yield of the compound (Y_r and Y_c) and the total ion current I_{tot} . Important in the context of this paper, is the parameter $(1-\varepsilon)$ that refers to the effective fraction of sputter material that arrives on the substrate. The fraction that is deposited on the target is given by ε . Similar arguments result in the derivation of the metal flux F_m .

The outgoing fluxes are defined by the deposition rate (bottom of Fig. 1). Indeed, the deposition of material on the substrate results in a transfer from the top layer toward the bulk of the deposited thin film. An example clarifies this reasoning. The deposition of a pure metal layer on the compound thin film can be seen as transferring compound from the top layer toward the bulk of the thin film. Hence the outgoing flux is controlled by the deposition rate d_s , which is defined by the average target condition [given by $\bar{\theta}_r$, $\bar{\theta}_c$, and $\bar{\theta}_m$, see further Sec. II C, Eq. (11)].

Finally we should account for the formation of compound material by the reaction between the reactive gas molecules and the deposited metal (left to right arrow in Fig. 1). This is a source term of compound and evidently a loss term of metal. The reaction is defined by the incorporation coefficient α_s (Ref. 12) and the flux of reactive gas molecules, given by Eq. (3). The number of reactive gas atoms per metal atom z defines the stoichiometry of the formed compound MR_z .

The reasoning above results in the following equation for compound fraction on the substrate θ_s :

$$n_{o,s} \frac{d\theta_s}{dt} = \frac{(1-\varepsilon)I_{\text{tot}}(Y_r \bar{\theta}_r + Y_c \bar{\theta}_c)}{A_s} (1-\theta_s) - \frac{(1-\varepsilon)I_{\text{tot}} Y_m \bar{\theta}_m}{A_s} \theta_s + \frac{2F}{z} \alpha_s (1-\theta_s), \quad (5)$$

with A_s the substrate area (cm^2) and $n_{o,s}$ the material surface density (at/cm^2). The metal fraction on the substrate is expressed as $(1-\theta_s)$.

From the substrate condition, the reactive gas consumption rate q_s [see Eq. (1)] toward the substrate can be calculated as^{7,9}

$$q_s = \alpha_s F (1-\theta_s) A_s. \quad (6)$$

Indeed, the consumption rate of the substrate is defined by the incorporation coefficient, and the flux of the reactive gas molecules. The consumption rate depends on the substrate area and the substrate condition, i.e., the fraction metal ($1-\theta_s$) present.

C. The target condition

A similar approach as for the vacuum chamber and the substrate is used for the target description. The model accounts for chemisorption of reactive gas molecules on the target, knock-on implantation of chemisorbed species, and direct reactive gas ion implantation. The reactive gas atoms are implanted in a region typically a few nanometer below the target surface.¹¹ For direct ion implantation, the molecular ions become neutralized just before the target surface, and upon implantation they split in two atoms. To account for these effects, the target is subdivided in 50 cells to describe the depth variation in the concentration of the compound, of the implanted reactive gas atoms, and of the nonreacted target material. Since the ion current density is nonuniform within the race track, the target is also subdivided in (10×25) cells to describe the ion current density distribution over the target surface. Hence, the target is described in detail by a $(10,25,50)$ matrix. At the surface, the three following materials can be present: nonreacted target material or metal, compound formed by chemical reaction with the implanted reactive gas atoms, and compound formed by chemisorption of reactive gas molecules at the surface. Here we assume that the two ways to form compound result in a compound with the same stoichiometry. However, as shown in Ref. 9, oxygen chemisorption affects the electron emission yield of an aluminum target in a different way than direct oxygen implantation. Hence, it can be important to distinguish between these two alternative pathways for compound formation.

Each material is represented by a given fraction in the target surface layer, i.e., $\theta_m^{i,j}$ represents the metal fraction, $\theta_r^{i,j}$ represents the compound fraction, and $\theta_c^{i,j}$ represents the compound fraction formed by chemisorption. The sum of these fractions is by definition equal to 1. The superscript (i,j) refers to the (x,y) position on the target. Each of these materials is characterized by a given sputter yield, Y_m , Y_r , and Y_c . Again continuity equations can be written for each of these materials. Figure 2 assists in the derivation of the first

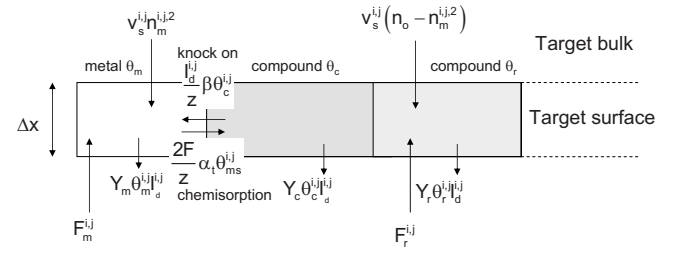


FIG. 2. (Color online) Schematic representation of the target surface description. Due to the target erosion at a given effective speed of v_s , target material is transferred from the bulk to the surface (see top arrows). This target material can be compound due to the reaction of the target material with implanted reactive atoms (see Fig. 3). Chemisorption of reactive gas molecules with a flux F converts target material θ_m into compound θ_c (arrow from left to right). The sticking coefficient α_t controls this reaction. Chemisorbed atoms can be knock-on implanted and therefore the compound is destroyed and metal is formed (arrow from right to left). The process is defined by the knock-on yield β and the ion current density I_d . Deposition of sputtered material on the target results in a flux of metal F_m and compound F_r toward the target which influences the effective erosion speed (bottom arrows pointing up). Each material is sputtered from the top surface (see bottom arrows pointing down) which is defined by their sputter yields and the ion current density I_d .

two equations. The last equation can be derived from these equations, knowing that the sum of the fractions should be equal to 1.

$$n_{o,s} \frac{d\theta_m^{i,j}}{dt} = v_s^{i,j} n_m^{i,j,2} - I_d^{i,j} Y_m \theta_m^{i,j} - \frac{2F}{z} \alpha_t \theta_m^{i,j} + \frac{I_d^{i,j}}{z} \beta \theta_c^{i,j} + F_m^{i,j},$$

$$n_{o,s} \frac{d\theta_r^{i,j}}{dt} = v_s^{i,j} (n_o - n_m^{i,j,2}) - I_d^{i,j} Y_r \theta_r^{i,j} + F_r^{i,j},$$

$$n_{o,s} \frac{d\theta_c^{i,j}}{dt} = \frac{2F}{z} \alpha_t \theta_m^{i,j} - \frac{I_d^{i,j}}{z} \beta \theta_c^{i,j} - I_d^{i,j} Y_c \theta_c^{i,j} - (F_r^{i,j} + F_m^{i,j}). \quad (7)$$

The metal fraction θ_m at the surface is defined by the erosion of the target (with v_s the target erosion rate) which transfers metal from the bulk to the surface [first term in Eq. (7)]. The metal is removed from the surface due to sputtering defined by the ion current density I_d and the metal sputter yield Y_m [second term in Eq. (7), bottom arrows pointing down in Fig. 2]. Also chemisorption of reactive gas molecules on the target results in a reduction in the target metal fraction as the metal is converted into compound [third term in Eq. (7), arrow from left to right in Fig. 2]. The sticking coefficient of the reactive gas molecules α_t on the metal and the flux of the reactive gas molecules F define this latter process. Due to the ion bombardment, chemisorbed atoms on the target surface can be implanted into the target [fourth term in Eq. (7), arrow from right to left in Fig. 2]. The ion current density and the knock on yield β control the rate of this process. Finally, deposition of metal on the target, given by the metal flux F_m , increases the metal fraction on the target surface [see last term in Eq. (7)].

For the compound fraction θ_r formed by reactive gas implantation at the target surface a similar reasoning can be made as for the metal fraction. Indeed, the erosion of the target transfers compound from the bulk to the surface (right top arrow in Fig. 2). Sputtering of the compound is defined

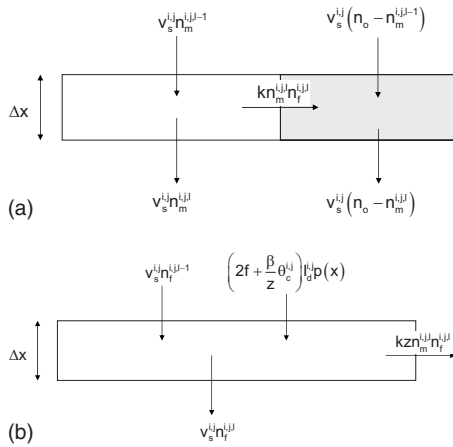


FIG. 3. Part (a) shows a bulk cell of the target. Compound and target material is transferred transversally toward the surface from one cell to another due to the target erosion at an effective speed v_s . Implanted nonreacted reactive gas atoms can react with the target material to form compound (left to right arrow). The reaction rate depends on the concentration of target material n_m , the concentration of implanted reactive atoms n_r , and the reaction rate constant k . A different target bulk cell is used to describe the implantation of reactive atoms [see part (b)]. The nonreacted reactive gas atoms are transferred from one cell to another due to the target erosion. Nonreacted reactive atoms become implanted according to the implantation profile $p(x)$ into the target by two mechanisms (top right arrow). The first is direct ion implantation which depends on the fraction f of reactive molecules in the plasma [see Eq. (4)]. The second is knock-on implantation, which has a yield β , and depends also on the target surface composition (θ_c). The implanted reactive atoms can react with the target material to form compound (left to right arrow).

by the ion current density I_d and the compound sputter yield Y_r (right bottom arrow pointing down in Fig. 2). Deposition of compound on the target, given by the compound flux F_r increases the compound fraction on the target surface.

The compound fraction θ_c is solely defined by surface processes. Indeed, the chemisorption of reactive gas molecules on the target surface is the only process resulting in an increase in this fraction. This process depends on the sticking coefficient α_t and the flux of the reactive gas molecules F (left to right arrow in Fig. 2). The formation process is balanced by sputtering characterized by the sputter yield Y_c (bottom middle arrow in Fig. 2), the knock on implantation (right to left arrow in Fig. 2) and the deposition of sputtered material on the target surface.

Equation (7) and Fig. 2 describe the target surface condition. For a description of the underlying layers, Eq. (8) and Fig. 3 should be used. In the bulk of the target three different species can be present as follows: metal, compound, and nonreacted implanted reactive atoms. The concentration of the metal is given by n_m . The concentration of the compound molecule is given by $(n_o - n_m)$ with n_o the initial metal concentration. Hence, in a first approximation it is assumed that the density in one lateral cell remains constant.

The concentration of the non reacted implanted atoms is given by n_r . Figure 3(a) describes the transversal transfer of the metal (n_m) and compound ($n_o - n_m$) from one cell to another due to the target erosion. Figure 3(b) depicts the implantation process, and the chemical reaction of the implanted reactive gas atoms (n_r) with the metal target atoms. Based on both figures, following equations can be derived:

$$\frac{dn_m^{i,j,l}}{dt} = v_s^{i,j} \nabla \cdot n_m^{i,j,l} - kn_m^{i,j,l} n_r^{i,j,l}, \quad (8a)$$

$$\frac{dn_r^{i,j,l}}{dt} = v_s^i \nabla \cdot n_r^{i,j,l} - zn_m^{i,j,l} n_r^{i,j,l} + \left(2f + \frac{\beta}{z} \theta_{cs}^{i,j}\right) I_d^{i,j} p(x). \quad (8b)$$

Equations (8a) and (8b) can be understood as follows. The concentration of the metal in a cell is defined by the transversal transfer process due to erosion [first term in Eq. (8a)], and the chemical reaction between the metal atoms and the implanted reactive atoms. This loss reaction is described by the second term in Eq. (8a) $kn_m^{i,j,l} n_r^{i,j,l}$, with k the reaction rate constant. The concentration of the nonreacted implanted reactive atoms also depends on the transfer process to the target erosion [first term in Eq. (8b)], and the reaction with the metal atoms [second term in Eq. (8b)]. Direct ion implantation and knock on implantation are the sources of reactive atoms in the bulk of the target [third term in Eq. (8b)]. Direct ion implantation depends on the fraction f of reactive molecules in the plasma [see Eq. (4)]. The second source is knock-on implantation, which has a yield β , and depends also on the target surface composition (θ_c). The atoms become implanted according the implantation profile $p(x)$ which is obtained from SRIM (see Sec. III A).

Important in the context of this paper is the effective erosion rate of the target v_s . When no deposition on the target occurs, the erosion speed at a given position on the target is defined by the ion current density and the target surface condition,

$$v_s^{i,j} = \frac{I_d^{i,j}(\theta_r^{i,j} Y_r + \theta_m^{i,j} Y_m + \theta_c^{i,j} Y_c)}{n_o}. \quad (9)$$

When deposition on the target occurs, this equation should be changed to

$$v_s^{i,j} = \frac{I_d^{i,j}(\theta_r^{i,j} Y_r + \theta_m^{i,j} Y_m + \theta_c^{i,j} Y_c)}{n_o} - \frac{I_{tot}(\bar{\theta}_r Y_r + \bar{\theta}_m Y_m + \bar{\theta}_c Y_c)}{n_o} \varepsilon^{i,j}, \quad (10)$$

i.e., the effective erosion rate is a balance between the sputter erosion of the target [see Eq. (9)] and the deposition on the target. The latter is defined by the average target condition (see below), and $\varepsilon^{i,j}$ the fraction of the sputtered particles arriving at the target surface cell with indices i and j , i.e., $\varepsilon = \sum_{i,j} \varepsilon^{i,j}$. In this way, the last term of Eq. (10) corresponds to the deposition rate at target position (i, j).

The average target condition defines the deposition rate and as such the substrate condition (see Sec. II B). To calculate the average target condition, the target condition of each surface cell (i, j) is weighted with the local ion current density. For the average compound fraction this results in the following equation:

TABLE I. Description and values of the used parameters in the model.

Parameter	Value	Origin
V, chamber volume	0.125 m ³	Experimentally determined.
S, pumping speed	111 L/s	Experimentally determined from argon pressure (0.3 Pa) and the argon flow (20 SCCM).
I _{tot} , discharge current	0.4 A	Experimental constant value.
P _{Ar} , argon pressure	0.3 Pa	Experimental constant value.
Y _m , sputter yield of the target material	0.65	Experimentally determined sputter yield for Al (at the discharge voltage of 400 V).
Y _r , sputter yield of the formed compound by reactive ion implantation	0.05	Experimentally determined sputter yield for Al ₂ O ₃ (Ref. 13). As the compound is assumed to be Al ₂ O ₃ , z is set equal to 1.5.
Y _c , sputter yield of the formed compound by chemisorption	0.05	Sputter yield for the compound formed by chemisorption. It is assumed that the compound stoichiometry is equal to Al ₂ O ₃ . Hence, the same sputter yield is used as for the compound formed by reactive ion implantation.
β, knock-on yield	0.2	Calculated using SRIM (Ref. 14).
p(x), Rp	1.5 nm	The implantation profile p(x) is described by a Gaussian. The ion range Rp is calculated using SRIM.
p(x), dRp	0.7 nm	The implantation profile p(x) is described by a Gaussian. The ion straggle dRp is calculated using SRIM.
α _s , incorporation coefficient for reactive molecules in the growing film	0.13	Experimentally determined (Ref. 12).
α _t , sticking coefficient of the reactive molecules on the target	0.13 0.01	The value was set equal to the incorporation coefficient for the region outside the race track. Inside the race track a lower value was used based on a previous study (Ref. 15).
k, reaction rate constant	4 × 10 ⁻²³ cm ³ s ⁻¹	The reaction rate constant is a fitting parameter as no experimental value can be found. Here the value was set equal to the value obtained by fitting several hysteresis experiments in a previous study (Ref. 9).
A _s , substrate area	1000 cm ²	A uniform deposition profile was assumed to reduce the calculation time. Hence, the latter value is a fitting parameter which has no relationship with the real substrate area.
ε, fraction of the sputtered material arriving on the target	0.13	Calculated using SIMTRA (Ref. 16).

$$\bar{\theta}_r = \frac{\sum_{ij} I_d^{ij} \theta_r^{ij}}{I_{tot} N}, \quad (11)$$

with N the total number of target surface cells (N = 10 × 25 = 250). Similar equations can be derived for $\bar{\theta}_m$ and $\bar{\theta}_c$.

III. EXPERIMENTAL RESULTS AND INPUT PARAMETERS

A. Input parameters

To describe the reactive behavior of the rotating cylindrical magnetron several input parameters are needed. Table I gives an overview of the parameters together with a short

description of the origin of the parameter. Figure 4 shows the experimental setup.

The target current density distribution was simulated using an electron trajectory code as presented in Ref. 13. The deposition profile on the target was simulated using SIMTRA. This code has been described in detail in Ref. 16, and it is a fast and accurate tool capable of handling complex geometries. In short, the code simulates the trajectory of a large amount of sputtered atoms. The atoms are released from the race track of the target. The collisions between the sputtered atoms and the argon gas are assumed to be elastic. The simulated deposition profile on the target is shown in Fig. 5(a). Important in the context of the paper is that the fraction of the sputtered material arriving on the target, ε (see Table I),

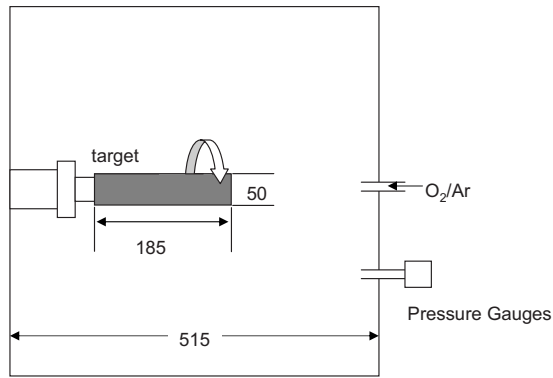


FIG. 4. Sketch of the experimental setup. The gray part represent the target. The pump is located in the middle of the backside of the vacuum chamber (not shown).

will depend on the experimental conditions. The location of the magnetron source in the vacuum chamber can play important role, and also the argon pressure has an important influence. The latter influence can be easily simulated using SIMTRA. The fraction ε increases almost linear from 0.027 at 0.1 Pa to 0.66 at 2 Pa. Hence, at high pressure a substantial fraction of the sputtered materials arrives back on the target. The erosion profile, as illustrated in Fig. 5(b), was simulated as described in Ref. 13.

B. Experimental results

The experimental parameters (discharge current, argon pressure, pumping speed, and target configuration) are described in Table I, and were taken from a previous study.⁸ Under these conditions, the reactive sputter behavior for different rotation speeds of the rotating cylindrical magnetron was studied. The rotation speed is expressed in rounds per minute (rpm). The oxygen flow was increased from 0 SCCM (standard cubic centimeters per minute) in steps of 0.1 SCCM until the target was completely poisoned. The latter was evaluated from a strong decrease in the discharge volt-

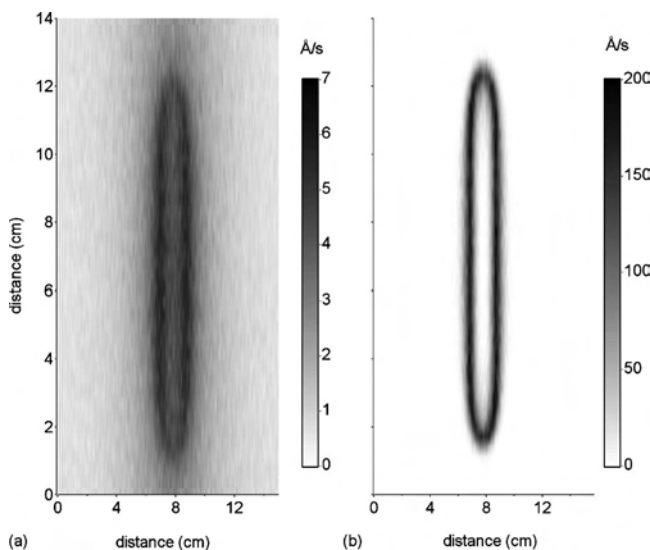


FIG. 5. (a) Deposition profile on the target calculated using SIMTRA (Ref. 16). (b) Simulated erosion rate on the rotating cylindrical magnetron (Ref. 13).

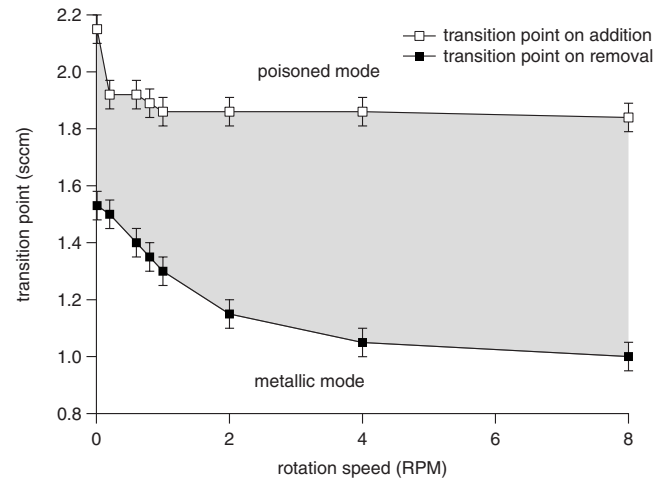


FIG. 6. Measured transition point on increasing and decreasing the oxygen flow as a function of the rotation speed of the rotating cylindrical magnetron.

age, which is characteristic for a poisoned aluminum target.¹² Between each step, a stabilization period of 3 min was respected. After fully poisoning the target, the oxygen flow was again stepwise decreased, respecting again the same stabilization period of 3 min. Figure 6 shows the experimental result for different values of the rotation speed. As mentioned before, the transition point for poisoning and de-poisoning depends on the rotation speed, and shifts toward lower values as the rotation speed increases. The behavior of the transition point on addition as a function of the rotation speed is different from that of the transition point on removal. For the first, the transition point drops abruptly to a lower oxygen flow when increasing the rotation speed at low rotation speeds but the influence of the rotation speed at higher rotation speed is minor. For the transition on removal of the oxygen, the influence of the rotation speed is more gradual.

IV. MODEL RESULTS AND DISCUSSION

A. Effect of the rotation speed

Using the input parameters given in Table I, the influence of the rotation speed on the hysteresis behavior of the rotating cylindrical magnetron was simulated. In a first series of simulations, deposition on the target was not included ($\varepsilon = 0$). Figure 7(a) shows the result. In contrast to the experiment, both transition points shift gradually to lower oxygen flows upon increasing the rotation speed.

In a second series of simulations, the deposition profile on the target, as depicted in Fig. 5(a), was included. As Fig. 7(b) shows, the experimental behavior is mimicked by the simulations, i.e., a sharp decrease in the transition point on oxygen addition toward lower oxygen flows when the target is rotated at a small rotation speed but at higher rotation speeds the influence on the transition point is minimal. The more gradual influence for the transition point on oxygen removal is also shown by the simulations.

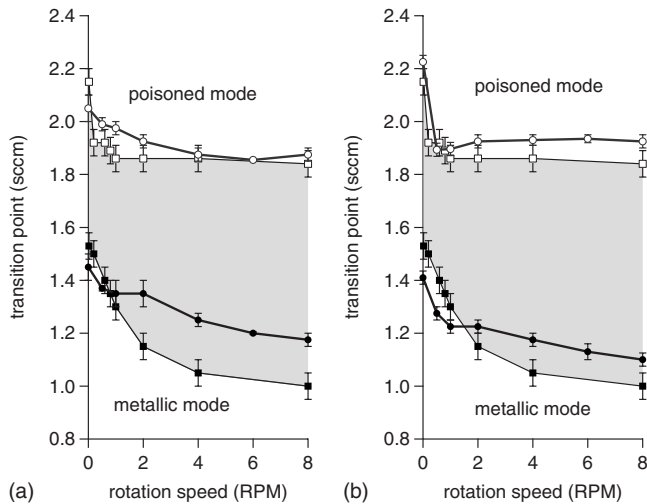


FIG. 7. The transition points on addition and removal of oxygen as a function of the rotation speed. Simulation results are given in thicker lines and round markers. The experimental data, adopted from Fig. 6, are represented by the thinner lines and square markers. In (a) the simulation does not include deposition of sputter material on the target. In (b) the simulation includes deposition of sputter material on the target.

B. Sputter cleaning of the target

A further testing of the simulation code can be performed by simulating another type of experiment. As discussed in Ref. 8, the target can be sputtered in oxygen/argon ambient in stationary mode. This will in turn result in deposition on the target. After a stabilization period of 2 min, the oxygen flow is switched off, and the target is rotated at a given rotation speed. Tracing the discharge voltage during this sputter cleaning of the target shows a periodic alternation of this parameter (see Fig. 8). The peaks can be interpreted based on the relative position of the plasma to the

stationary race track. For position 1 (see Fig. 8) the plasma coincides with the complete stationary race track position. In position 2, only one side of the stationary elliptical race track corresponds to the plasma. In position 3, the stationary race track stands straight across the plasma, while in position 4, the other side of the race track coincides with a side of the plasma. As the high discharge voltage is typical for the metallic mode during aluminum sputtering and a low discharge voltage is typical for the poisoned mode, the simulated behavior of the average metal fraction on the target surface should correspond with the discharge voltage behavior. As discussed before, the average metal fraction is the metal fraction on the target weighted according the ion current density. Hence, it resembles the target condition of the target in the race track. As Fig. 8 shows, the correspondence between experiment and simulation is good when deposition on the target is included but is poor when the influence of deposition on the target is omitted.

The behavior of position 2, 3, and 4 will be sensitive to the thickness of the deposited layer on the target. When the stationary target is sputtered in metallic mode, i.e., at an oxygen flow lower than the first transition point, the deposition rate is high, and a thick layer will be formed on the target. In contrast, the layer will be thin when the target is sputtered in poisoned mode. This is illustrated in Fig. 9, showing the simulated oxide fraction in the first 2.5 nm (eight monolayers) of the target after 30 s of sputtering in stationary mode. One notices that at low oxygen flow (left figure) the target is not poisoned as a low target oxide fraction is noticed in the race track position (located at 135° and 225°). Outside the race track the target contains a considerable oxide fraction up to a depth of 1.5 nm under the target surface due to the high deposition rate. On the other hand, when the oxygen flow is high, the target is completely poi-

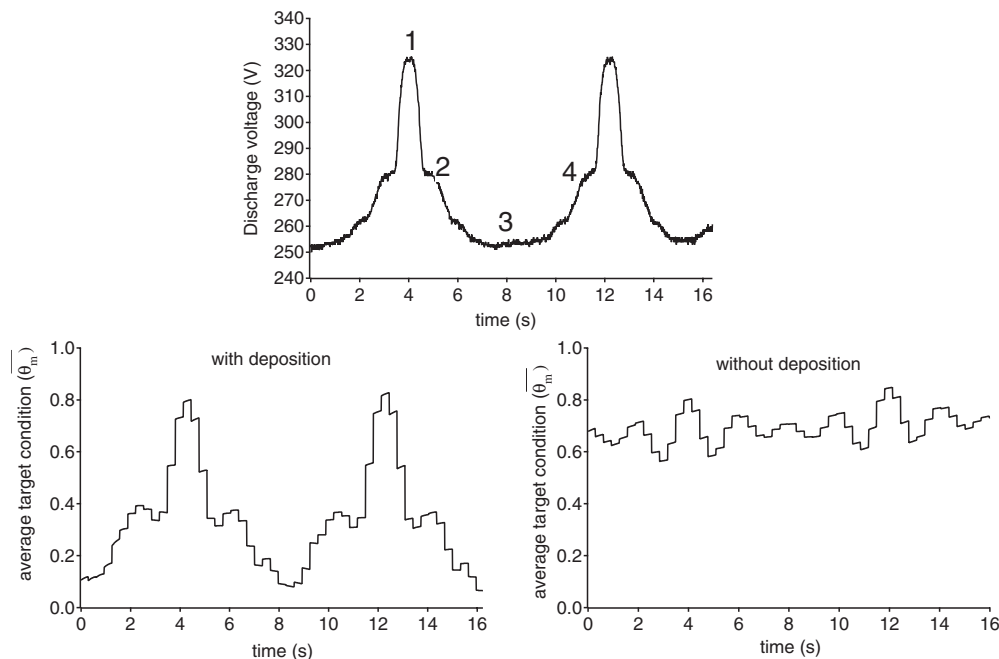


FIG. 8. Sputter cleaning of a target sputtered in stationary mode. The target was sputtered in metallic mode with an oxygen flow of 1.8 SCCM. After two minutes of stabilization the target was sputter cleaned in pure argon at a rotation speed of 7.5 rpm. The experimental results are shown in the top graph. The simulations are shown in two bottom graphs.

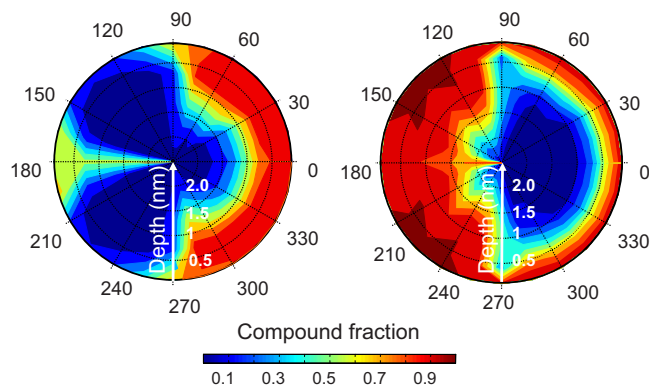


FIG. 9. (Color online) Polar plot of the compound fraction as function of the target depth and the position on the target (angular coordinate) after 30 s of sputtering the target in stationary mode. This cross section of the target was taken halfway the target (see Fig. 5, 7 cm on the vertical axis). The race track is located at 135° and 225° . For the left figure the oxygen flow was set at 1.8 SCCM, i.e., lower than the transition point for poisoning. For the right figure the oxygen flow was set at 2.4 SCCM resulting in the poisoning of the target.

poisoned in the race track position (right figure) but due to the low deposition rate only 0.6 nm of the target outside the racetrack contains a considerable oxide fraction.

This difference in oxidation state of the target affects the sputter cleaning behavior. The latter was investigated experimentally in Ref. 8. Figure 10 compares experiment with simulation. Again a good correspondence is found, indicating that the kinetics of the reactive sputter experiments are quite well described.

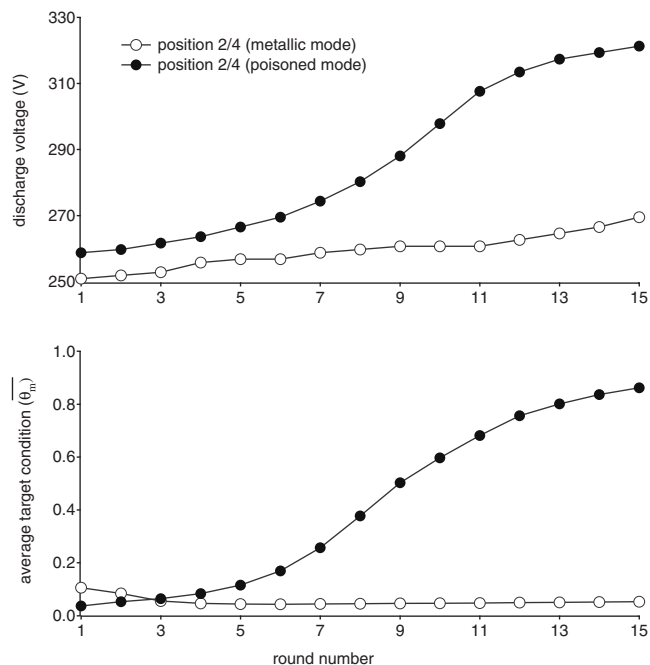


FIG. 10. The behavior of the measured discharge voltage (top) related to position 2/4 (see description in text and peaks indicated in Fig. 8) as a function of the number of target rotations during sputter cleaning of the target. The stationary target was first sputtered in metallic (1.8 SCCM O_2) or in poisoned mode (2.5 SCCM O_2) for 2 min (open and full symbols, respectively). Then the oxygen flow was switched off, and the target was sputtered cleaned in pure argon while rotating at 7.5 rpm. The simulation (bottom) was performed under the same conditions as the experiment (top), and the target condition was followed during sputter cleaning of the target, i.e., in the simulation the oxygen flow was set equal to zero after 120 s.

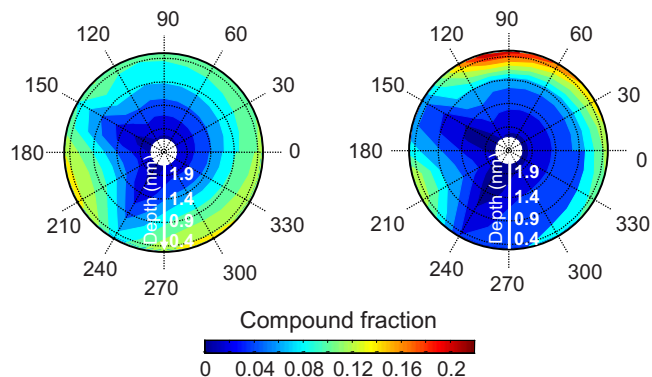


FIG. 11. (Color online) Simulation of the target oxidation state without (left) and with (right) deposition. For both situations the target rotation speed was set at 6 RPM counter clockwise and the oxygen flow was fixed at 2 SCCM.

C. Understanding the influence of the deposition

Including deposition of the sputtered material on the target is essential for the understanding of the reactive sputtering behavior of rotating cylindrical magnetrons. When this deposition is not included, the shift in the transition points to lower oxygen flows can be explained by oxygen chemisorption on the target.⁵ During its rotation the target surface outside the race track reacts with oxygen due to chemisorption and even at low oxygen pressure, a given target part will reach a high oxidation level. The rotation speed of the target will hardly influence the oxidation state as reaching a fully oxidized target surface by chemisorption is much faster than the rotation period. Indeed, to reach an oxidation state of 95%, only 1.95 s are needed at a typical reactive gas partial pressure of 5×10^{-3} Pa before the transition point. On entering the racetrack the oxide layer will be sputtered. At low rotation speed, the target surface will be completely sputter cleaned before the surface element rotates out of the race track. However, at higher rotation speed the residence time of a given surface element in the race track will be smaller, and complete removal of the oxide layer will not occur. Hence, the target will poison at lower oxygen flows for a higher rotation speed. Similar arguments hold for the de poisoning mechanism. When including the deposition on the target, the poisoning mechanism changes drastically. At low rotation speeds, the residence time of a target surface element in the race track is longer but the layer deposited on the target will be thick. When increasing the rotation speed, the thickness of the deposited layer will become smaller but the residence time in the racetrack will also decrease proportionally. Hence, the influence of the rotation speed on the first transition point will be small as shown by the experiment and the simulation. For the transition point on reactive gas removal, the influence of the deposition is much smaller as the deposition rate is drastically reduced by target poisoning. Hence, a similar behavior as without deposition will be noticed.

This difference between both simulations, i.e., with and without deposition, can also be illustrated by looking to the cross section of the target. Figure 11 shows the target oxidation state below the target surface, i.e., from 0.4 nm up to 2.1 nm. Without deposition (left) the oxide fraction is solely de-

fined by reactive ion implantation, and therefore hardly changes when rotating out of the racetrack. The small decrease in the target oxidation state outside the racetrack is due to the asymmetry of the erosion profile. With deposition (right) a clear increase in the oxide fraction is noticed when rotating out of the racetrack. Hence at the position just before entering the race track (between 90° and 120°) a higher compound fraction is found than at the position just outside the racetrack (between 270° and 300°).

V. CONCLUSIONS

The behavior of a rotating cylindrical magnetron during reactive magnetron sputtering was successfully simulated by including the deposition of sputtered target material on the target. At low oxygen flows, this results in the formation of an oxide layer which drastically influences the target behavior. The influence of the rotation speed is minimal except for very low rotation speeds where the balance between the growth of the deposited layer outside the racetrack and the sputter removal of the deposited layer in the racetrack can still be influenced by the rotation speed. Once the target is completely poisoned, the deposition rate is substantially reduced, and the influence of the deposition is much lower.

ACKNOWLEDGMENTS

This work was supported by the Institute for the Promotion of Innovation through Science and Technology in Flanders (IWT-Vlaanderen) and the FWO-Flanders.

¹M. Wright and T. Beardow, *J. Vac. Sci. Technol. A* **4**, 388 (1986).

²W. De Bosscher and D. Cnockaert, "Advances in Cylindrical Magnetrons," 41st Society of Vacuum Coaters Annual Technical Conference Proceedings, 1999, pp. 156–162.

³P. A. Greene and R. Dannenberg, "Modeling of Production Scale Reactive Deposition of a Cylindrical Magnetron," 43rd Society of Vacuum Coaters Annual Technical Conference Proceedings, 2000, pp. 127–132.

⁴A. W. Smith, N. G. Butcher, D. Walker, "Reactive Sputtering from a Dual Rotatable Cathode for SiO₂, Si₃N₄ and SiO_xN_y Coatings onto Flexible Substrates," 45th Society of Vacuum Coaters Annual Technical Conference Proceedings, 2002, pp. 113–118.

⁵O. Kappertz, T. Nyberg, D. Rosén, and S. Berg, "Influence of Rotating Magnets on Hysteresis in Reactive Sputtering," 47th Society of Vacuum Coaters Annual Technical Conference Proceedings, 2004, pp. 271–275.

⁶D. Depla, J. Haemers, G. Buyle, and R. De Gryse, *J. Vac. Sci. Technol. A* **24**, 934 (2006).

⁷D. Depla, S. Heirwegh, S. Mahieu, and R. De Gryse, *J. Phys. D: Appl. Phys.* **40**, 1957 (2007).

⁸X. Y. Li, D. Depla, W. P. Leroy, J. Haemers, and R. De Gryse, *J. Phys. D: Appl. Phys.* **41**, 035203 (2008).

⁹D. Depla, S. Mahieu, and R. De Gryse, in *Reactive Sputter Deposition*, Springer Series in Materials Science Vol. 109, edited by D. Depla and S. Mahieu (Springer, New York, 2008).

¹⁰RSD2009 can be downloaded from www.draft.ugent.be

¹¹J. Affinito and R. R. Parsons, *J. Vac. Sci. Technol. A* **2**, 1275 (1984).

¹²W. P. Leroy, S. Mahieu, R. Persoons, and D. Depla, *Plasma Processes Polym.* **6**, 342 (2009); W. P. Leroy, S. Mahieu, R. Persoons, and D. Depla, *Thin Solid Films* **518**, 1527 (2009).

¹³A. Bogaerts, E. Bultinck, I. Kolev, L. Schwaederle, K. Van Aeken, G. Buyle, and D. Depla, *J. Phys. D: Appl. Phys.* **42**, 194018 (2009); D. Depla, S. Mahieu, and R. De Gryse, *Thin Solid Films* **517**, 2825 (2009).

¹⁴SRIM can be downloaded from www.srim.org

¹⁵D. Depla and R. De Gryse, *Surf. Coat. Technol.* **183**, 196 (2004).

¹⁶K. Van Aeken, S. Mahieu, and D. Depla, *J. Phys. D: Appl. Phys.* **41**, 205307 (2008); SIMTRA can be downloaded from www.draft.ugent.be